

Breaking Surface Wave Effects on River Plume Dynamics during Upwelling-Favorable Winds

GREGORY P. GERBI

Skidmore College, Saratoga Springs, New York

ROBERT J. CHANT AND JOHN L. WILKIN

Rutgers, The State University of New Jersey, New Brunswick, New Jersey

(Manuscript received 27 September 2012, in final form 17 May 2013)

ABSTRACT

This study examines the dynamics of a buoyant river plume in upwelling-favorable winds, concentrating on the time after separation from the coast. A set of idealized numerical simulations is used to examine the effects of breaking surface gravity waves on plume structure and cross-shore dynamics. Inclusion of a wave-breaking parameterization in the two-equation turbulence submodel causes the plume to be thicker and narrower, and to propagate offshore more slowly, than a plume in a simulation with no wave breaking. In simulations that include wave breaking, the plume has much smaller vertical gradients of salinity and velocity than in the simulation without breaking. This leads to decreased importance of shear dispersion in the plumes with wave breaking. Much of the widening rate of the plume is explained by divergent Ekman velocities at the off- and onshore edges. Some aspects of plume evolution in all cases are predicted well by a simple theory based on a critical Richardson number and an infinitely deep ocean. However, because the initial plume in these simulations is in contact with the sea floor in the inner shelf, some details are poorly predicted, especially around the time that the plume separates from the coast.

1. Introduction

Under the influence of upwelling-favorable winds, buoyant plumes separate from the coast and travel offshore, eventually mixing with water on the shelf (Csanady 1978; Xing and Davies 1999; Fong and Geyer 2001; Houghton et al. 2004; Lentz 2004). Their evolution depends on winds and on the dynamics of the surface boundary layer (Xing and Davies 1999). Coincident with, but distinct from, studies of buoyant plumes in recent years, parameterizations have been developed and implemented that attempt to parameterize the effects of whitecapping surface gravity waves on upper-ocean turbulence (Craig and Banner 1994; Burchard 2001; Carniel et al. 2009). Because these parameterizations are relatively new, limited descriptions of their dynamical effects on regional circulation have been

developed (Carniel et al. 2009; Zhang et al. 2011). In this study, we examine buoyant plumes under upwelling-favorable winds. Using a numerical model, we study how the inclusion of a wave-breaking parameterization affects the evolution of the buoyant plume. The analysis includes examination of some of the findings of Fong and Geyer (2001) and Lentz (2004) for the case of no wave breaking and a study of how the plume dynamics change with wave breaking. We first introduce turbulence in the surface boundary layer and then give background on Fong and Geyer (2001) and Lentz (2004).

a. Turbulence from wave breaking

Turbulence in the surface boundary layer is driven by at least three processes: surface stress, wave breaking, and Stokes drift shear instabilities. Circulation models use two-equation closures (e.g., k - ϵ) or vertical profile [e.g., K -profile parameterization (KPP)] submodels to parameterize turbulent mixing near the surface. These models traditionally have included the effects of momentum and buoyancy flux through the sea surface

Corresponding author address: Greg Gerbi, Departments of Physics and Geosciences, Skidmore College, 815 North Broadway, Saratoga Springs, NY 12866.
E-mail: ggerbi@skidmore.edu

(Jones and Launder 1972; Mellor and Yamada 1982; Large et al. 1994). Surface gravity waves affect surface boundary layer dynamics through wave–current interaction, Stokes shear instabilities, and wave breaking. A straightforward parameterization of wave breaking has been developed and implemented in numerical models (Craig and Banner 1994; Burchard 2001; Carniel et al. 2009). This parameterization is improved by but does not require full simulation of the wave field and is relatively simple to include in simulations. Schemes to include wave–current interaction and effects of Stokes drift are more complicated and less well developed, although progress continues to be made (Uchiyama et al. 2010; Kumar et al. 2012; McWilliams et al. 2012). In this study, we examine the effects of the wave-breaking parameterization of Craig and Banner (1994) as modified by Burchard (2001) on buoyant plume evolution.

The effects of waves and wave breaking on turbulence in the ocean surface boundary layer have been studied through observations (Agrawal et al. 1992; Anis and Moum 1995; Gemmrich et al. 1994; Terray et al. 1996; Gerbi et al. 2008, 2009; Gemmrich 2010), analytic models (Craig 1996; Burchard 2001; Ardhuin et al. 2008; Teixeira 2012), and large-eddy simulations (Noh et al. 2004; Sullivan et al. 2007; McWilliams et al. 2012). These studies have shown that turbulent kinetic energy (TKE) density, dissipation rates of turbulent kinetic energy, turbulent diffusivity, and turbulent viscosity are all enhanced beneath breaking surface waves relative to what would be expected for turbulence at a rigid boundary. This results in a more uniform vertical distribution of properties in the surface boundary layer than would be expected without breaking waves.

The parameterization of Craig and Banner (1994) and Burchard (2001) treats wave breaking as a source of turbulent kinetic energy at the sea surface and changes the roughness length at the surface. It has been shown to be consistent with observations in several one-dimensional studies of turbulence, momentum, and tracers (Terray et al. 1996; Drennan et al. 1996; Soloviev and Lukas 2003; Stips et al. 2005; Gerbi et al. 2008, 2009). In a recent three-dimensional model of the Adriatic Sea, Carniel et al. (2009) showed that the tracks of surface drifters were more accurately reproduced by models that included this wave-breaking parameterization in the turbulence closure than by models that did not include wave breaking. Similarly, Zhang et al. (2011) showed that including the wave-breaking parameterization improved simulation of the surface boundary layer thickness in the Yellow Sea. The study presented here examines the effects of wave-breaking turbulence on the dynamics and evolution of a coastal system in an idealized numerical experiment. Specifically, this study

addresses the evolution of a buoyant coastal plume under upwelling-favorable conditions with and without wave breaking.

b. Buoyant coastal plumes in upwelling-favorable winds

Under the influence of upwelling-favorable winds a coastal plume will separate from the coast and move offshore, continually thickening and widening (Fong and Geyer 2001; Houghton et al. 2004; Lentz 2004). Building on the work by Fong and Geyer (2001), Lentz (2004) proposed an analytic theory to predict the thickness, width, and mean density of a buoyant plume as it moves offshore. The essential dynamics of this theory are lateral straining and vertical mixing at the plume front (offshore edge), and vigorous lateral and vertical mixing within the plume, to maintain horizontally uniform density and velocity and deliver freshwater to the plume front. The controlling parameter in this theory is a critical bulk Richardson number that parameterizes the turbulent mixing at the plume front. The bulk Richardson number is defined as

$$R_b = \frac{g\Delta\rho h}{\rho_r|\Delta u|^2}, \quad (1)$$

where h is plume thickness, $\Delta\rho$ is the mean density difference between ambient water and the plume, ρ_r is a reference density of the water, Δu is the mean velocity difference between the plume and the waters beneath the plume, and g is the acceleration due to gravity. The theory is based on simple assumptions of a well-mixed slab-like plume, no alongshore variations, and an infinitely deep coastal ocean. It predicts

$$h = h_0(1 + \hat{t})^{1/3}, \quad \Delta\rho = \Delta\rho_0(1 + \hat{t})^{-1}, \quad \text{and} \\ X = W_i + \int_0^{\hat{t}} dt \frac{U_E}{h}, \quad (2)$$

where W_i is initial plume width, X is the offshore position of the plume front, $U_E = \tau/\rho_r f$ is the Ekman transport, τ is the wind stress, f is the Coriolis frequency, t is time, and \hat{t} is time normalized by the time needed for the plume to double in cross-sectional area. The values h_0 and $\Delta\rho_0$ denote thickness and density difference immediately after the onset of wind. The offshore propagation speed of the plume front dX/dt is a function only of Ekman transport and plume thickness. For plumes that do not immediately detach from the coast, the plume width is a two-part function

$$W = X, \quad t \leq t_{\text{sep}}; \quad W = W_0(1 + \hat{t})^{2/3} \quad \text{and} \quad t > t_{\text{sep}}, \quad (3)$$

where t_{sep} is the time that the plume separates from the coast and is itself an output from the theory, and W_0 is a function of initial conditions.

Lentz (2004) showed that, using a critical bulk Richardson number of 1, the theory did a reasonable job of predicting the results of the numerical model from Fong and Geyer (2001) and of the evolution of an observed coastal plume off the North Carolina coast under weak to moderate winds. The theory does not account explicitly for breaking waves, but because the bulk Richardson number represents unresolved turbulent processes, parts of the model might be applicable to simulations with breaking waves. Such application would likely require a different critical bulk Richardson number.

Lentz's theory was developed for a vertical coastal wall and assumed a plume with uniform thickness. Fong and Geyer's numerical model was run with a deep coastal wall, but the plume in their simulation was not of uniform thickness. In this paper we use numerical experiments to examine plume dynamics in general, revisiting the results of Fong and Geyer (2001) and Lentz (2004) in a region with a sloping bottom. We then examine both qualitatively and quantitatively the effects of breaking waves on plume evolution. Section 2 describes the model, reviews turbulence closure and the parameterization of wave breaking, and describes the metrics used in this study. Section 3 describes plume evolution and differences between simulations with and without wave breaking, and section 4 discusses changes in the internal dynamics with the addition of wave breaking. Section 5 offers conclusions.

2. Methods

a. Numerical model, forcing, and initial conditions

This study examines the effects of wave breaking on plume evolution using the Regional Ocean Modeling System (ROMS; <http://www.myroms.org>). ROMS is a hydrostatic primitive equation model with a terrain-following σ -coordinate stretched vertical grid. Its computational kernel has been described by Shchepetkin and McWilliams (2005, 2008) and Haidvogel et al. (2008) [as corrected by Shchepetkin and McWilliams (2009)]. The model was used with no horizontal mixing of tracers or momentum.

This study uses an idealized coastal domain with constant upwelling-favorable winds. The domain is similar to that used by Jurisa and Chant (2013) and is about 280 km along-shelf by 230 km across-shelf (120 km of river and 110 km of ocean, Fig. 1). For convenience, the coast is oriented north-south with the ocean to the

east and land to the west. Southerly and easterly directions are referred to as downshelf and offshore, respectively. Cross-shelf resolution varies from about 625 m near the river mouth to a maximum of 1.7 km near the offshore edge. Along-shelf resolution varies from about 180 m near the mouth to almost 2 km at the downshelf boundary. In the vertical dimension the stretched grid gives fine resolution near the surface, moderate resolution in middepths, and coarse resolution near the bottom. Vertical resolution varies with water depth and is tens of centimeters near the surface in shallow water. The model has a straight river of 10-m depth and 120-km length opening onto a straight continental shelf with slope of 0.001. The river discharge is a constant $1500 \text{ m}^3 \text{ s}^{-1}$, representing a moderate springtime runoff event in the Hudson River (see Choi and Wilkin 2007). The incoming river water was distributed uniformly with depth at the upstream end of the river. The model has a 10-m coastal wall and the shelf slopes continuously to the edge of the model domain at 120-m depth at 110-km offshore. We chose this wall depth to maintain numerical stability near the river mouth and for the possibility of comparison with the work of Jurisa and Chant (2013). Section 4d discusses possible effects of this wall in comparison to a model domain that continues to shallower water.

Initial conditions were the same for all cases in this study and were generated by running the model from a state of constant salinity in the ocean and linear stratification in the estuary. The model ran for 20 days with tidal forcing, river input, and along-shelf flow at the boundaries (see below), but no wind. A large bulge region formed at the river mouth, and a coastal current extended downstream (Fig. 1). At the location of the transects examined for this study (mean downshelf distance from river mouth of 96 km), the coastal current carried about 45% of the river freshwater transport, with the remainder going into the growing bulge at the river mouth.

Radiation conditions are used at the open boundaries (Flather 1976; Chapman 1985) and incorporate tidal forcing and mean along-shelf flow. Tides are specified through free surface elevation and depth-mean flow at the eastern (offshore) boundary using only the M_2 tide. Tidal velocities at the river mouth are about 0.5 m s^{-1} . Along-shelf flow is specified using a modification of the formulation of Lentz (2008) at the northern and southern boundaries (Zhang et al. 2009). Depth-mean downshelf flow is proportional to the water depth with flow of 0.025 m s^{-1} at the coast and 0.1 m s^{-1} at the offshore edge of the domain.

Using these initial and boundary conditions, an upwelling-favorable (northward) wind stress is ramped

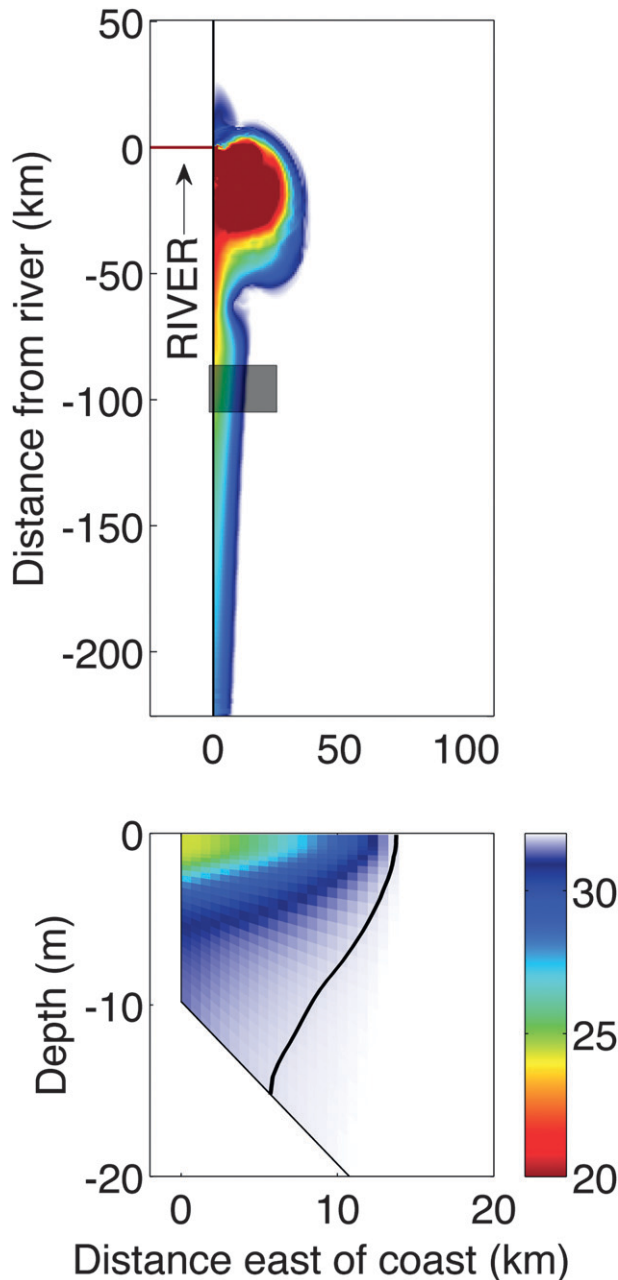


FIG. 1. Plume initial conditions. (top) Map view of salinity at 1-m depth is shown. (bottom) Initial cross section of salinity is shown. The alongshore extent of the gray band in the top shows the alongshore extent averaged in the analysis, and the cross-shore extent of the gray band shows the cross-shore extent of the cross section shown in the bottom. The black line in the bottom is the contour of 31.9 psu, which was used to define the base of the plume.

from 0 to 0.1025 Pa over 1.7 h [following Fong and Geyer (2001)]. The simulations last between 3.5 and 6.5 days, depending on how quickly the plume front reaches the model boundary. All the simulations use the k - ε

turbulence closure model (Jones and Launder 1972; Rodi 1980). They differ only in whether the wave-breaking parameterization is included and in the values of two terms in that parameterization (see below).

b. Turbulence closure and breaking waves

In common two-equation turbulence closure models [see Burchard and Bolding (2001), Umlauf and Burchard (2003), and Umlauf and Burchard (2005) for more details and references], vertical turbulent viscosity K_m and turbulent diffusivity K_t are parameterized as

$$K_m = \frac{c_\mu}{(c_\mu^o)^{3/4}} q l \quad \text{and} \quad K_t = \frac{c'_\mu}{(c_\mu^o)^{3/4}} q l, \quad (4)$$

where q^2 is the turbulent kinetic energy density, l is a turbulent length scale, c_μ^o is a constant model parameter, and c_μ and c'_μ are stability functions for momentum and tracers, respectively. The length scale l is proportional to the maximum size of energy-containing eddies. Together, l and q give the dissipation rate of TKE ε :

$$\varepsilon = (c_\mu^o)^{3/4} \frac{q^3}{l}. \quad (5)$$

This combination of terms leads to alternate representations of turbulent viscosity and diffusivity:

$$K_m = c_\mu \frac{q^4}{\varepsilon} \quad \text{and} \quad K_t = c'_\mu \frac{q^4}{\varepsilon}. \quad (6)$$

During integration of a numerical model, at each time step evolution equations are solved for q^2 and l and values of c_μ and c' are determined from nondimensional vertical gradients of density and velocity. Then, (4) is evaluated to provide turbulent diffusivities to the evolution equations for momentum and tracers. There are several versions of the stability functions (see Burchard and Bolding 2001), and this study uses the formulations of Kantha and Clayson (1994). There are also several common forms of the evolution equation for l , each of which solves an equation for $q^{m/n}$, with different parameters m and n (see Umlauf and Burchard 2003; Warner et al. 2005). The k - ε turbulence closure model solves an evolution equation for ε by using $m = 3$ and $n = -1$.

The simulations in this study do not resolve surface gravity waves. Instead, wave breaking is parameterized in the turbulence closure model following the approach of Craig and Banner (1994), Burchard (2001), and Umlauf and Burchard (2003) as implemented in ROMS

by Warner et al. (2005) and Carniel et al. (2009). In the absence of wave breaking, the surface boundary condition for q^2 is no flux through the boundary, and the surface boundary condition for l is that it has a minimum value, a roughness length z_0 , which is usually on the order of a centimeter. When wave breaking is included, changes are made to the flux of TKE through the sea surface and to the roughness length. The surface TKE flux is meant to equal the rate at which energy is taken from the wave field and converted to turbulence by breaking. The surface roughness length is increased by a factor of 10–100 over what would be found at a rigid boundary, allowing much larger turbulent length scales at the sea surface. TKE flux through the sea surface is parameterized as

$$K_q \frac{\partial q^2}{\partial z} = G_t u_*^3, \quad (7)$$

where K_q is the turbulent diffusivity for TKE defined in a way similar to (4), $u_* = \sqrt{\tau/\rho_r}$ is the friction velocity, and G_t is a model parameter. This energy flux parameter G_t is likely a function of wave age and sea state (Terray et al. 1996). Observations have found values of G_t between 80 and 250 (Feddersen et al. 2007; Jones and Monismith 2008; Gerbi et al. 2009). The surface roughness length z_0 has also been difficult to constrain and is likely a function of wave height (Terray et al. 1996) or wavelength (Drennan et al. 1996). Several studies have found under limited conditions that z_0 may be linearly proportional to the significant height of the wind waves H_s , with $0.5H_s \lesssim z_0 \lesssim 1.3H_s$ (Terray et al. 1999; Burchard 2001; Jones and Monismith 2008; Gerbi et al. 2009). Carniel et al. (2009) use a Charnock-type relationship to define z_0 , which is similar to assuming a linear relationship between wind stress and H_s . In this study, results are shown for eight simulations that vary both the surface roughness length z_0 and the TKE flux from the wave field to the turbulence (by varying the energy flux parameter G_t). One control case is made with no wave breaking, with $G_t = 0$ and $z_0 = 0.014$ m. Five cases use values of G_t and z_0 meant to span the observed parts of parameter space. Two cases only incompletely adopt the wave-breaking parameterization and are made with a wave-breaking value for only one parameter and a standard (no breaking) value for the other. The parameters z_0 and G_t are held constant in each simulation (Table 1).

These simulations do not account for all possible wave effects on turbulence and wave–current interactions. Unaddressed effects include Coriolis–Stokes forcing (Hasselmann 1970; Polton et al. 2005), Stokes shear production of turbulent kinetic energy (Uchiyama et al.

TABLE 1. Summary of simulations. Cases 2 and 6 only partially adopt the wave-breaking parameterization.

Case	G_t	z_0 (m)	Description
1	0	0.014	Basic case
2	150	0.014	Moderate wave energy input, standard (no wave) roughness length
3	150	0.31	Moderate wave energy input, small roughness length
4	150	0.61	Moderate wave energy input, moderate roughness length
5	150	0.92	Moderate wave energy input, large roughness length
6	0	0.61	No wave energy input, wave-breaking-sized roughness length
7	100	0.61	Small wave energy input, moderate roughness length
8	200	0.61	Large wave energy input, moderate roughness length

2010; Kumar et al. 2012; McWilliams et al. 2012), and wave radiation stress (Warner et al. 2008; Uchiyama et al. 2010). Ignoring those processes reduces the complexity of this study and allows us to determine whether even a simplistic, easily applied parameterization has consequences for regional circulation. In addition, properly incorporating those more complicated wave effects would require a more realistic simulation of the wave field and would increase the number of parameterizations involved.

c. Computation of plume statistics

To quantify the differences between simulations, four bulk plume metrics are examined along with vertical structure of the plume. The metrics are mean plume thickness, mean plume density, plume width at the surface, and the offshore position of the plume’s leading edge. These quantities are computed using a mean cross-shore section computed from 20 grid cells in the along-shore direction (about 20 km), with the section’s center 96 km from the center of the river. Shelf salinity S in the model initial condition is 32. The plume is defined as water with salinity less than 31.9. In cross-shelf sections, there are occasionally multiple boluses of low-salinity water ($S < 31.9$) separated by high-salinity water ($S > 31.9$) (see section 3a). The offshore bolus is always the best defined and freshest, and when multiple boluses are present plume statistics are computed from the one that is farthest offshore.

At each offshore position, plume thickness is computed from the distance between the free surface and the bottom of the deepest grid cell containing water with $S \leq 31.9$. Mean plume thickness is the horizontal average of plume thicknesses. Vertical grid resolution near the

plume base varies with location but is usually about 1–2 m. Plume width is the distance between the outside edges of the surface grid cells with $S \leq 31.9$. Mean density difference is computed from the density difference between the plume water and the water immediately below the plume. Cross-sectional area of the plume is not shown but can be computed as the product of plume width and mean thickness. Prior to calculation of plume thickness, density difference, width, and position of the offshore edge of the plume, the salinity field was interpolated onto a grid with 200-m horizontal resolution. Vertical resolution was kept constant. This smoothing changed the horizontal resolution by a factor between 3 and 8 depending on cross-shore location.

The plume centroid and second horizontal moment are computed using the distribution of the freshwater concentration F :

$$F = \frac{S_0 - S}{S_0}, \quad (8)$$

where $S_0 = 32$. The x centroid is defined as

$$\bar{x} = \frac{\int_{x_n}^{x_f} dx x \int_{z_b}^0 dz F}{\int_{x_n}^{x_f} dx \int_{z_b}^0 dz F}, \quad (9)$$

where x_n is the horizontal position of the onshore (trailing) edge, x_f is the horizontal position of the offshore (leading) edge, and z_b is the plume base at position x . The z centroid is similarly defined as

$$\bar{z} = \frac{\int_{x_n}^{x_f} dx \int_{z_b}^0 dz z F}{\int_{x_n}^{x_f} dx \int_{z_b}^0 dz F}. \quad (10)$$

The second horizontal moment is

$$x_m^2 = \frac{\int_{x_n}^{x_f} dx (x - \bar{x})^2 \int_{z_b}^0 dz F}{\int_{x_n}^{x_f} dx \int_{z_b}^0 dz F}. \quad (11)$$

Rates of change of quantities are computed as

$$\left. \frac{dx}{dt} \right|_n = \frac{x_{n+1} - x_{n-1}}{t_{n+1} - t_{n-1}}, \quad (12)$$

where n denotes a sample number, and samples are spaced with 1-h resolution. Because of variability in computed derivatives, these are filtered with a non-causal low-pass boxcar filter with a window length of 24 h.

The Richardson number theory by Lentz (2004) predicts plume evolution based on wind stress and plume initial conditions. It assumes an initially triangular shape against the coastal wall that evolves to a rectangular shape with a flat bottom immediately after the onset of wind. We made two sets of comparisons to the theory, both using a bulk Richardson number equal to 1. For the most complete comparison, initial plume width and density were computed directly from the initial conditions. Because the initial shape in the simulations is not triangular, initial plume thickness h_i is computed as $h_i = 2A_i/W_i$, where A_i is the initial cross-sectional area of the plume. The other set of comparisons between the simulations and Lentz's theory initialized the theory 10 h after the plume had separated from the coast using the simulated thickness, density difference, width, and cross-sectional area for h_0 , $\Delta\rho_0$, W_0 , and A_0 , respectively (where A_0 is the cross-section area after onset of winds).

Vertical salt flux by turbulence is not a model output in ROMS, so it had to be calculated from other diagnostic quantities of the model. ROMS output does include the mean vertical derivative of vertical salt flux for each grid cell. The difference in vertical salt flux between the top and bottom of each grid cell is computed as the product of the vertical derivative and the thickness of each cell. Finally, the salt flux is computed as the cumulative sum of the vertical differences, using zero salt flux through the sea floor.

3. Results

a. Plume evolution

After the onset of winds, the buoyant plume in each case widens and begins to move offshore (Figs. 2 and 3). In the first half-day after onset of wind, the mean depth of each plume base decreases as the plume water adjusts to the upwelling-favorable wind (Fig. 4). After less than one day, the base of the plume in all simulations has evolved from being initially steeply sloped to a much more gently sloped state that is slightly shallower at the leading (offshore) edge of the plume than at the trailing (onshore) edge.

After 25–40 h (depending on the simulation), the buoyant plume detaches from the coast. As it detaches, the plume leaves behind some freshwater in the inner shelf. This occurs in water depths shallower than about

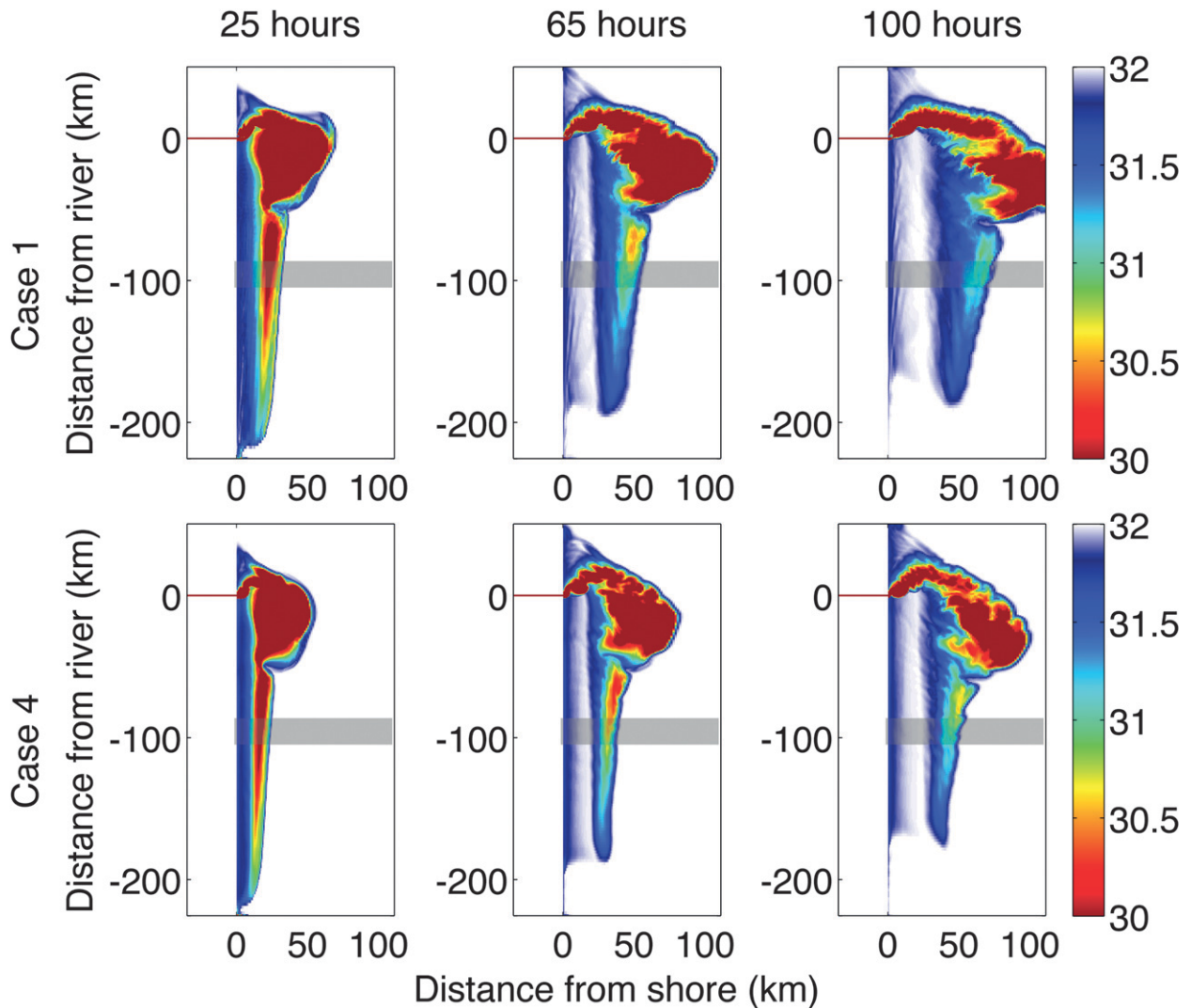


FIG. 2. Map views of salinity at 1-m depth with wave breaking (top) turned off (case 1) and (bottom) turned on (case 4). Times are measured from the beginning of nonzero wind stress. The gray bar shows the area used to define cross sections of the plume.

1.5 times the theoretical Ekman layer thickness (computed using the mean turbulent viscosity) and considerably less than the vertical length scale $\kappa u_* / f$ suggested by Madsen (1977) (with κ as the von Kármán constant). The limited cross-shelf circulation near the shore is consistent with the predictions of Ekman (1905) and observations of Fewings et al. (2008) that, in the inner shelf, along-shelf winds are least able to drive cross-shelf circulation. In the real ocean, buoyant plumes do not often leave behind freshwater in this manner, but the model does not contain cross-shelf winds or parameterizations of surface wave processes that could drive cross-shelf flows (Fewings et al. 2008; Lentz et al. 2008). The detachment process and leaving behind of freshwater causes sharp jumps in the

measured density and width of the plume and a smaller jump in mean plume thickness. The evolution of the offshore position of the plume front has no discontinuity (Fig. 4). In the results of Fong and Geyer (2001) freshwater is not left behind near the shore, most likely because their model has a much deeper coastal wall and effectively eliminates the inner shelf.

As discussed in more detail by Fong and Geyer (2001) and Lentz (2004), as the upwelling-favorable winds continue, the river plume moves offshore and both thickens and widens. The increased cross-sectional area of the plume leads to an increased mean density of the plume water (decreased $\Delta\rho$). Initially, alongshore variability in the plume downstream of the bulge was restricted to scales on the order of the model domain size.

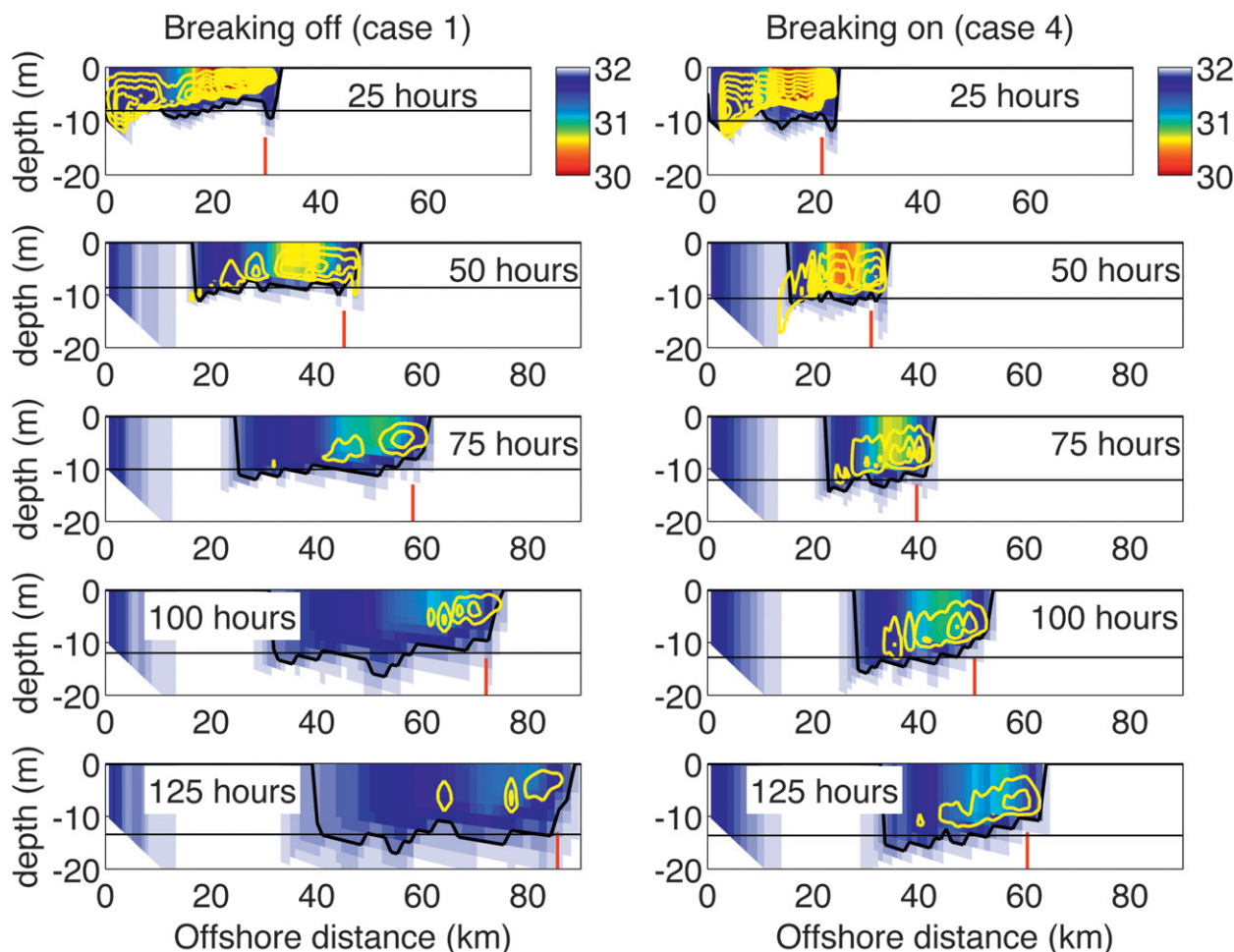


FIG. 3. Cross-shelf sections of plume evolution with wave breaking (left) turned off (case 1) and (right) turned on (case 4). Times are measured from the beginning of nonzero wind stress. In each cross section, the thick black line is the plume base z_b lying between waters of salinity greater than and less than 31.9 psu. The thin horizontal line is the mean plume depth. Thin yellow contours are vertical salt flux by turbulence (interval of 1×10^{-5} psu $m s^{-1}$). The outermost contour in each plot is 1×10^{-5} psu $m s^{-1}$. Along the bottom edges, the red vertical line segments show the cross-shore position one deformation radius inshore of the plume's leading edge (computed using mean plume density and thickness).

After the onset of wind, however, alongshore variability on smaller scales becomes more noticeable (Fig. 2). This causes minor variations in the plume properties unrelated to the two-dimensional evolution discussed in the remainder of this study. This variability is weak, however, and the dominant alongshore variability occurs on length scales much wider than the width of the cross section averaged in this study.

Within the plume, salt is transported vertically by turbulence across most of the width of the plume in simulations with and without wave breaking. This vertical mixing of salt is concentrated in the offshore half and is somewhat correlated with regions of large salinity gradient (as might be expected in a gradient transport model; Fig. 3). This is consistent with the results of Fong

and Geyer (2001). The relationship between the location of the salt flux within the plume and the location of entrainment of water into the plume is not immediately obvious. Lentz (2004) suggests that the entrainment occurs within one deformation radius of the plume's offshore edge and is redistributed by lateral and vertical mixing. However, if lateral mixing is limited, the entrainment may occur at the same cross-shore locations as the vertical salt flux. This would suggest that entrainment occurs across about half of the plume width.

b. Effects of wave breaking

This study focuses on times after the plume has detached from the coast (1–2 days after onset of wind). The simulations were not designed to examine in detail the

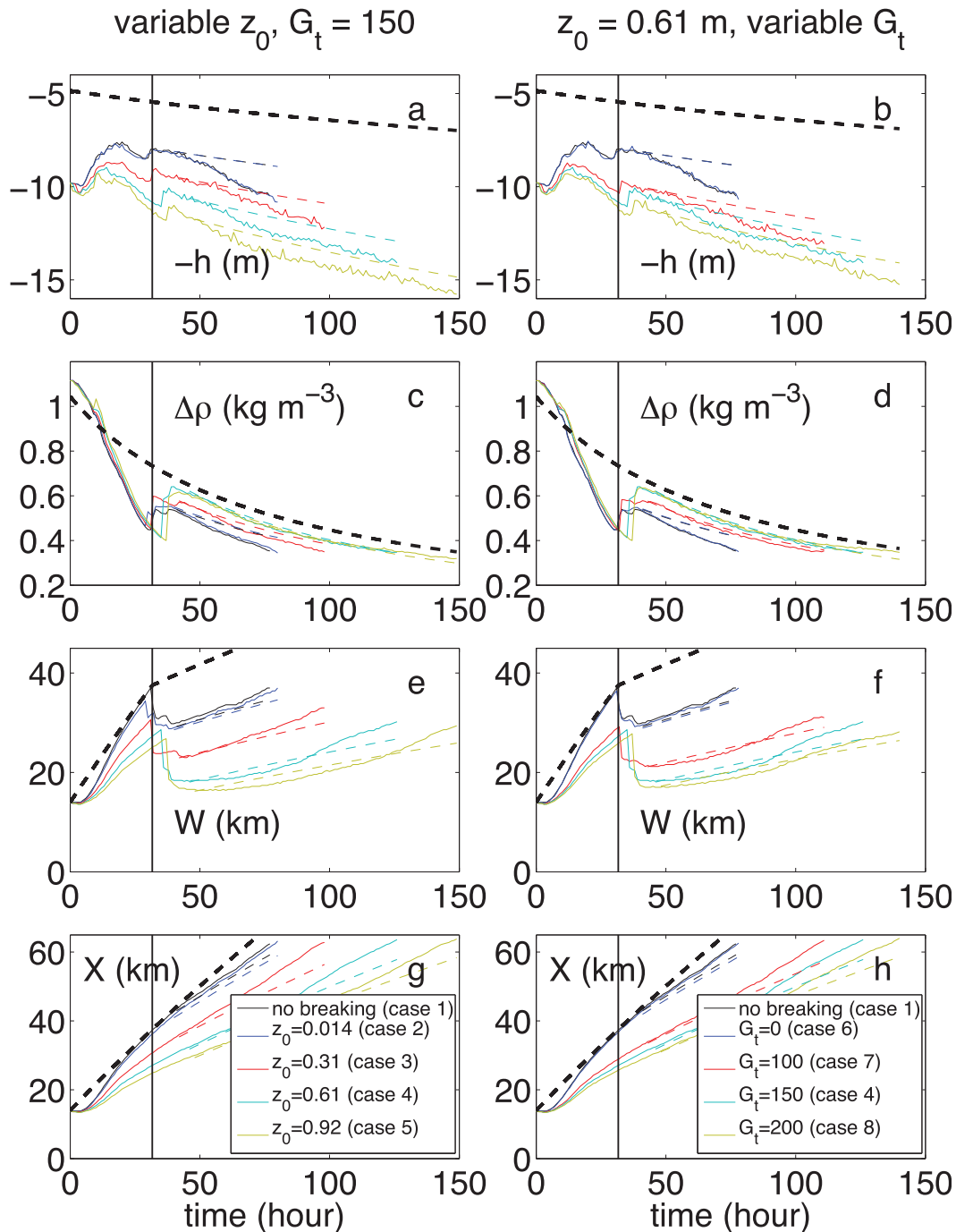


FIG. 4. Plume dimensions. (a),(b) Mean thickness; (c),(d) mean density difference from water beneath plume; (e),(f) plume width at surface; and (g),(h) offshore position of plume front. (left column) Variations caused by changing the roughness length z_0 and holding the TKE flux and G_t constant. (right column) Variations caused by varying the magnitude of TKE flux across the surface (by changing G_t) and holding the roughness length constant. Black lines (nearly indistinguishable from blue lines) have no wave breaking ($z_0 = 0.014$ m, $G_t = 0$). Blue lines represent cases with incomplete adoption of the wave-breaking parameterization. Cyan lines are the same in both columns. Dashed lines are predictions using the bulk Richardson number theory of Lentz (2004) with $R_b = 1$. The thicker black dashed line uses the initial conditions of the simulation as the initial conditions of the theory. The thinner colored dashed lines use the plume conditions 10 h after separation from the coast as the initial conditions of the theory with the exception of h_0 , which is set to the plume thickness. The vertical line is the separation time predicted by the theory using the simulation initial conditions.

time prior to detachment, which would require more detailed simulation of the wave field and wave–current interaction. At the time of separation from the coast, the plume in the simulation without wave breaking is thinner than the plume in simulations with wave breaking, by about 50% of the no-breaking thickness (Figs. 4a,b). The plume thickens at different rates in each of the simulations. After separation from the coast, the plume in the simulation without wave breaking deepens more quickly than the plume in the simulations with wave breaking. (Figs. 5a,b).

The plume thickness affects the rate at which the plume moves offshore because the wind stress is required to move more water in the case of a thicker plume (Lentz 2004). This causes the plume in the simulation without wave breaking to move offshore at a rate considerably higher than (as much as double) the rate of offshore motion of the plume in the simulations with wave breaking (Figs. 5g,h).

The plume widths are also different immediately after separation from the coast, with wave-breaking simulations having a narrower plume than the no-breaking simulation. The differences in width increase in time. In the no-breaking simulation, the plume continues to widen at rates larger than those in the simulations with breaking (Figs. 5e,f).

The mean density anomaly of the plume is a function of the amount of water entrained into the plume. The differences in cross-sectional area (not shown) between the breaking and no-breaking cases are substantial, but the majority of the differences arise during separation from the coast. Following separation, the mean density anomaly in the absence of wave breaking decreases only slightly faster than the mean density anomaly in the simulations with wave breaking (Figs. 5c,d).

Because wave breaking is parameterized by the addition of TKE at the sea surface, the wave-breaking simulations have higher TKE densities than the simulations without wave breaking (Figs. 6a,b). The dissipation rate of TKE is also increased with wave breaking, but the effect is somewhat modulated by the increased turbulent length scales (5) related to the increased roughness length (Figs. 6c,d). The changes in TKE density and dissipation rate lead to increases in turbulent diffusivity and viscosity (6) of roughly an order of magnitude in the presence of wave breaking (Figs. 6e,f). The increases in turbulent viscosity and diffusivity lead to decreases in vertical gradients of the cross-shelf velocity u , and the salinity (Fig. 7). The magnitude of the momentum flux is constrained by the wind stress, so the increase in turbulent viscosity and the decrease in velocity gradient largely balance each other and do not lead to increased momentum transport in the plume.

c. *Effects of details of wave-breaking parameterization*

Within the range of parameters used to define the wave-breaking simulations, there are quantitative, but not substantial qualitative, differences in the results. The main tunable parameters in these simulations of wave breaking are the magnitude of TKE flux through the sea surface and the surface roughness length. Recall that the roughness length is likely proportional to the significant wave height (Terray et al. 1996), so that changes in z_0 can be thought of as reflecting changes in H_s . Similarly, many different values of G_t have been estimated from observations (Terray et al. 1996; Feddersen et al. 2007; Jones and Monismith 2008; Gerbi et al. 2009) and it is likely a function of the sea state, with the highest values coinciding with moderately developed seas (Terray et al. 1996). To understand the effects of each parameter, each physical mechanism is examined independently.

If one makes only a half-step toward including wave breaking by changing only one of either the TKE input or the roughness length, very little change is evident in the plume evolution compared to the no-breaking case (cf. blue and black lines in Fig. 4). However, some changes are evident in the turbulent quantities (Fig. 6) that are similar to those found by Carniel et al. (2009) in an idealized, periodic channel model. Allowing TKE flux through the boundary while maintaining a small roughness length leads to increased TKE density and increased dissipation rates, and slightly increased turbulent viscosities and diffusivities. Alternatively, increasing the roughness length without allowing TKE flux through the sea surface decreases the dissipation rate slightly, as predicted by (5). This leads to increased turbulent diffusivity (6). Even with the decreased dissipation rate, the magnitude of TKE in the boundary layer remains largely unchanged.

In contrast to varying only roughness length or TKE input, increasing both to provide a more realistic parameterization of the effects of wave breaking causes substantial changes in plume evolution. Both the TKE flux and the increased roughness length are important, and varying either one within reasonable ranges for the ocean leads to similar changes in plume width, thickness, and density. If TKE flux through the boundary is held fixed, then increasing the roughness length leads to increases in turbulent viscosity and diffusivity (Fig. 6, left column). Similarly, if the roughness length is set to an appropriate value, then increasing the TKE flux through the boundary also leads to increases in turbulent viscosity and diffusivity (Fig. 6, right column). One minor difference is evident in the turbulent quantities for the two threads of this experiment. For a fixed value of G_t ,

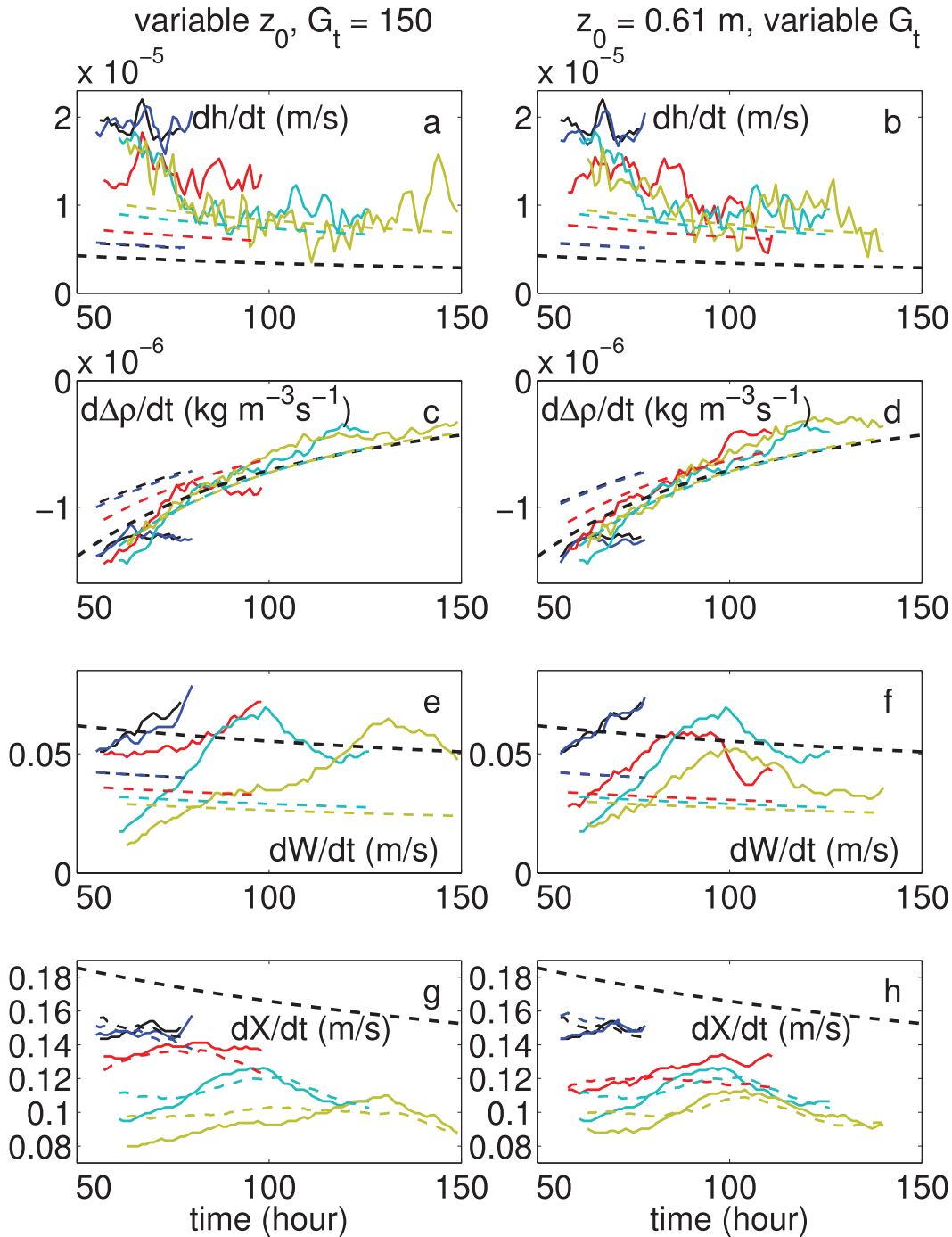


FIG. 5. As in Fig. 4, but for rate of change of plume properties. In (g),(h), the thinner dashed lines show dX/dt estimated as the cross-section Ekman transport U_E divided by modeled depths 1000-m inboard of the plume front at each time step. The data are filtered with a 24-h boxcar filter. The earliest time shown is the time of separation from the coast plus 24 h. The latest time shown is the time that the plume began to feel the effects of the offshore edge of the model domain.

when the roughness lengths are increased, the dissipation rates in the uppermost grid cells decrease (Figs. 6c,d). This is a direct result of (5), and causes TKE densities to increase because less TKE has been dissipated.

Increasing the TKE flux through the sea surface while keeping z_0 fixed at 0.61 m also leads to increased TKE density and to larger dissipation rates at all depths. In this case the increased TKE is caused by the injection of

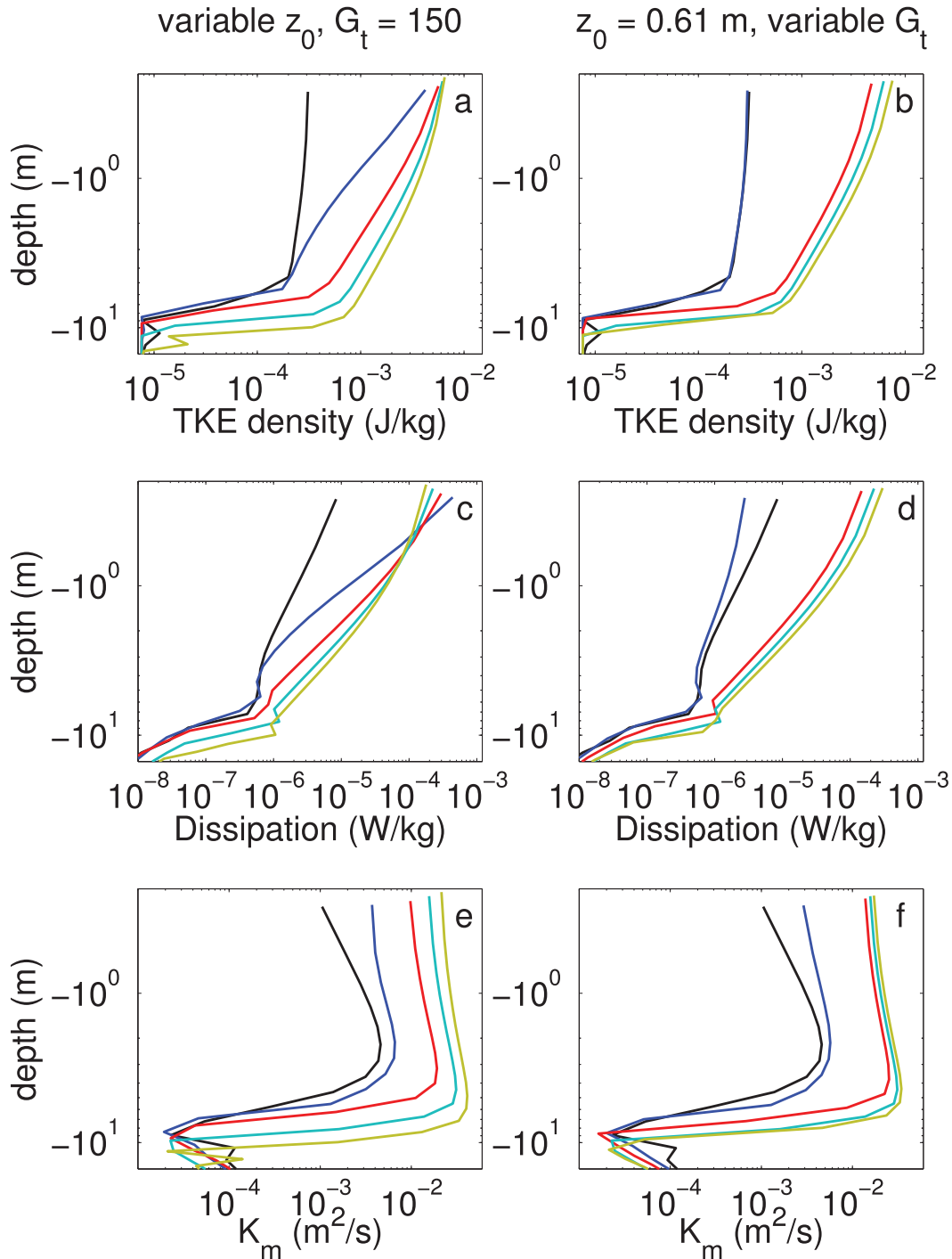


FIG. 6. Profiles of plume properties taken at the offshore location of the min surface salinity 65 h after the onset of wind. (a),(b) TKE density; (c),(d) dissipation rate of TKE; and (e),(f) turbulent diffusivity. (left column) Variations caused by changing the roughness length and (right column) variations caused by changing the magnitude of TKE flux across the surface are shown. Same colors as in Fig. 4.

additional TKE, and not by a lack of dissipation. In both sets of simulations, increasing either the roughness length or the TKE input from wave breaking increases turbulent viscosities and diffusivities.

Plume dimensions and cross-shore location are also affected by the details of the turbulence parameterization (Figs. 4 and 8). At all times after the onset of winds, the simulations with larger wave-breaking parameters

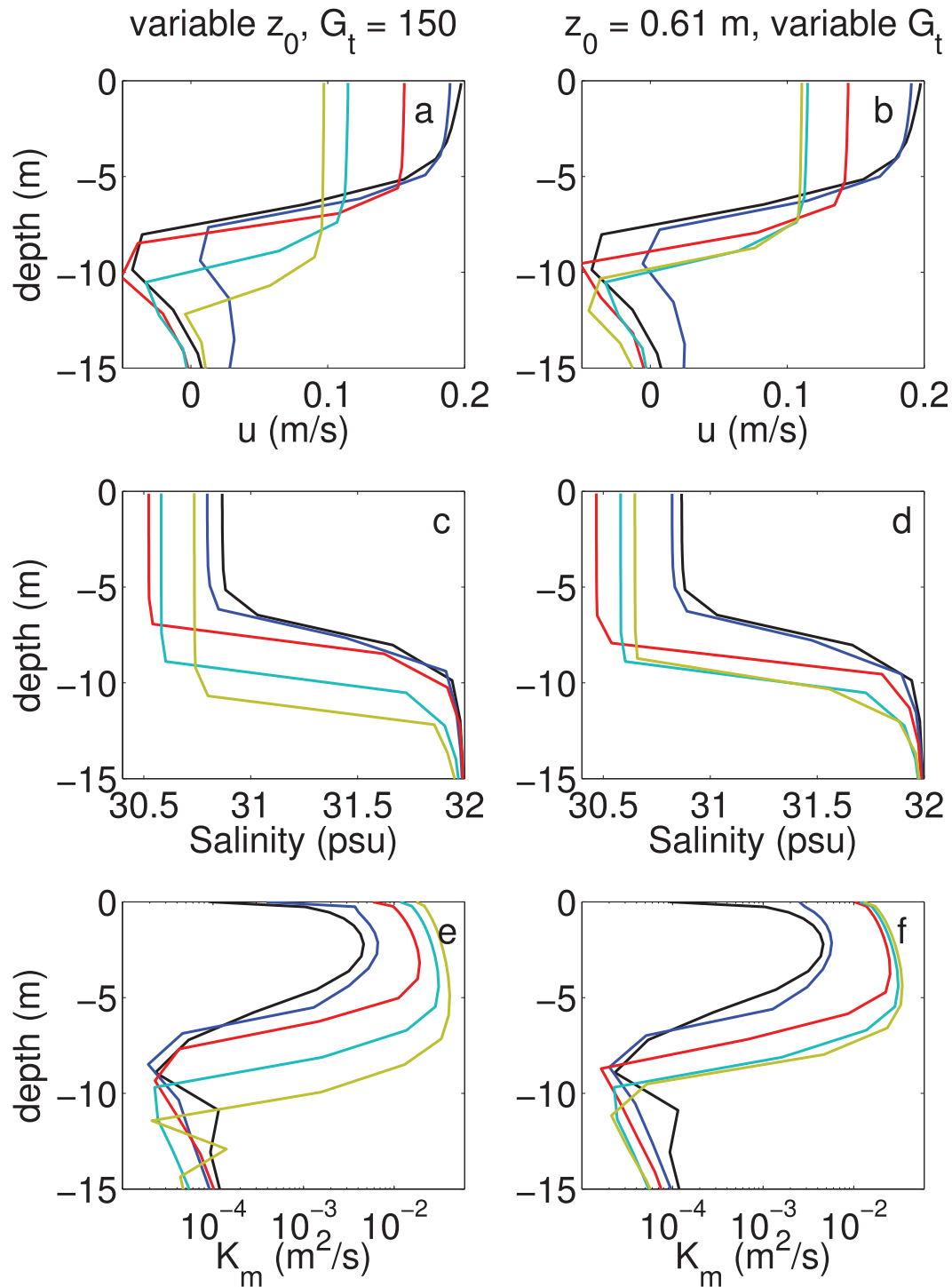


FIG. 7. Profiles of plume properties taken at the offshore location of the min surface salinity 65 h after the onset of wind. (a),(b) Cross-shelf velocity; (c),(d) salinity; and (e),(f) turbulent viscosity. (left column) Variations caused by changing the roughness length and (right column) variations caused by changing the magnitude of TKE flux across the surface are shown. Same colors as in Fig. 4.

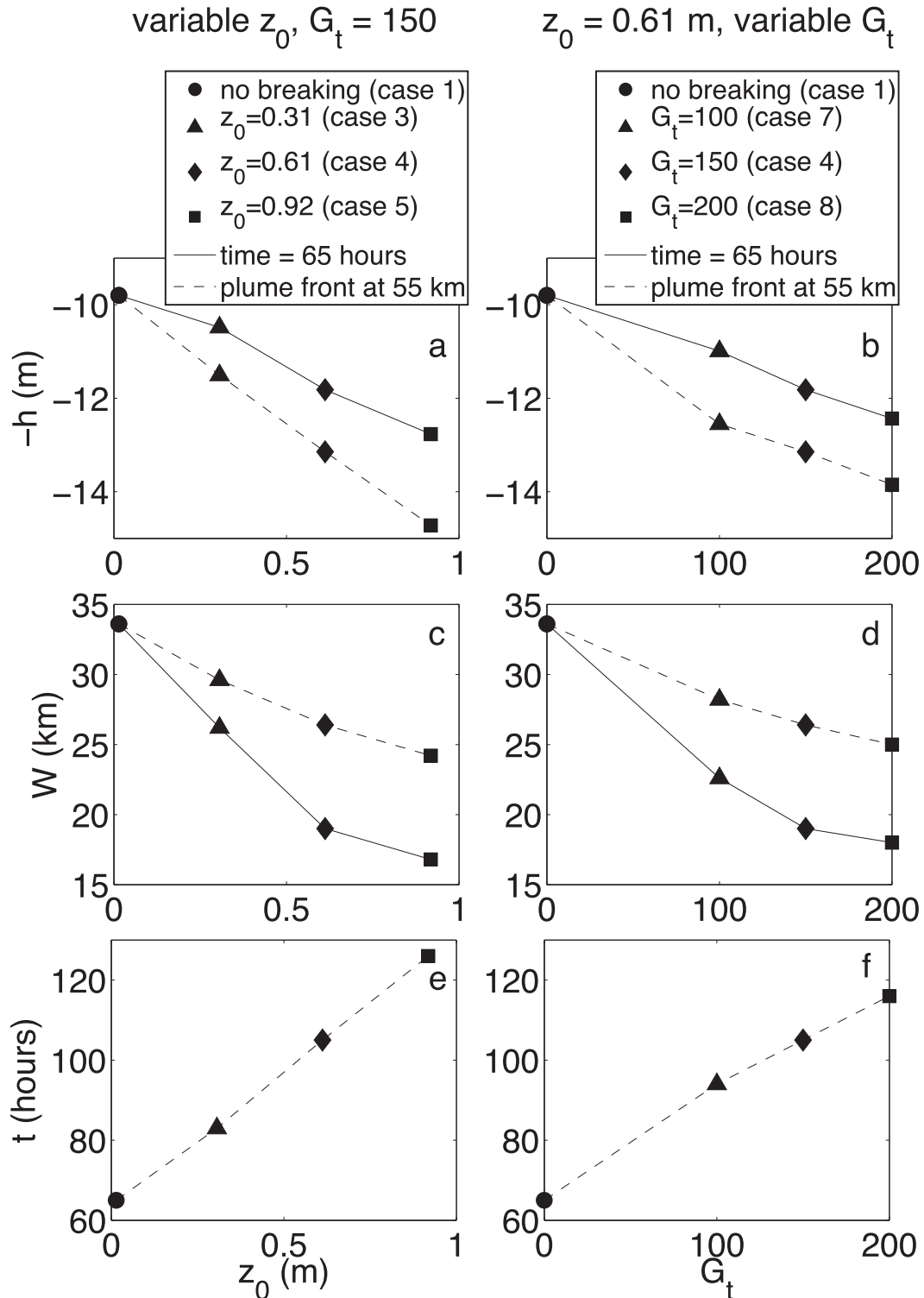


FIG. 8. Comparison of mean plume properties at fixed times (solid lines) and fixed offshore positions (dashed lines). (a),(b) Mean plume thickness; (c),(d) plume width; and (e),(f) time are shown. (left column) Variations caused by changing the roughness length and (right column) variations caused by changing the magnitude of TKE flux across the surface are shown. Solid lines show properties 65 h after the start of the simulation. Dashed lines show properties when the plume front is 55 km offshore. Symbols differentiate the parameters in the turbulence closure.

(larger TKE input or larger roughness length) are thicker and narrower, and their offshore edges are less far from the coast. Similarly, after the plume front has propagated to an arbitrary distance from the coast, the simulations with larger wave-breaking parameters are thicker and narrower (Fig. 8). For the simulations with wave breaking (cases 3, 4, 5, 7, and 8), the plume under the most energetic breaking is 10%–20% thicker and from $\frac{2}{3}$ to $\frac{1}{2}$ of the width of the plume under the least energetic breaking. Because offshore propagation speed is related to plume thickness, the rate at which the plume moves offshore is also sensitive to the details of the wave-breaking parameterization. The plume with the least energetic breaking moves offshore about 30% faster than the plume with the most energetic wave breaking. Similarly, the offshore front of the plume with no wave breaking travels offshore about twice as fast as the plume in the most energetic breaking case. In addition to likely consequences for cross-shore transport and exchange, this has practical importance in models with narrow cross-shore domains and suggests that the turbulence parameterization can influence whether a plume is likely to propagate out of the model domain.

4. Discussion

a. Comparison with bulk Richardson number theory

Some aspects of plume evolution are predicted well by the theory of Lentz (2004): X , $\Delta\rho$ after separation, and W prior to separation, all for the simulation with no wave breaking. Other aspects are not predicted well by the theory: h , $\Delta\rho$ before separation, and W after separation, for all simulations (Fig. 4). One critical aspect of the theory that compares favorably to the simulations is the assumption that the rate at which the plume moves offshore can be predicted as

$$\frac{dX}{dt} = \frac{U_E}{h}. \quad (13)$$

After separation from the coast, if the simulated thickness of the plume front is used in that comparison rather than the predicted thickness, then the agreement between theory and simulations is good in most simulations (Figs. 5g,h). After separation, the theory has some skill in predicting the rates of density and thickness changes, but interestingly, the theory does a better job for the simulations with wave breaking than the one without wave breaking. The theory has little skill at predicting the rate of change of plume width (Figs. 5e,f).

The fact that the simulated rates of plume thickening are almost always larger than the rate predicted by the

theory (starting with the simulation initial conditions at $t = 0$) suggests that water is entrained into the plume at a much larger rate in the simulations than is accounted for in the theory. This is consistent with the notion that entrainment occurs over a larger fraction of the plume base than the narrow region near the front suggested by Lentz (2004). One might expect this enhanced entrainment to correspond to values of $d\Delta\rho/dt$ larger than the theoretical prediction. However, because the plume is thicker in the simulations than in the theory, the enhanced entrainment rates are required for agreement between simulated and predicted $d\Delta\rho/dt$ as shown by

$$\frac{d\Delta\rho}{dt} = -\frac{A_0\Delta\rho_0}{w_e h^2 W}, \quad (14)$$

which can be derived by considering conservation of volume and mass. In the no-breaking case, the plume is thicker and narrower than predicted by factors of about 2. This allows the entrainment rate to be twice as large as the prediction without affecting the rate of change of plume density.

One difficulty in comparing the simulations to the theory is that the theory is written for an infinitely deep ocean. There are geometric changes associated with this limitation but also dynamic ones. The geometry can be handled in a straightforward way following Lentz's derivation but using a sloping bottom. Additional parameters describing the bottom slope and initial slope of the plume front are necessary. If the initial plume width, cross-sectional area, and depth are held constant, this modification has only minimal effects that are caused by changing the cross-sectional area of the fluid that is entrained immediately after the onset of winds. The time that the plume separates from the coast in the modified theory is slightly later than the time in the unmodified theory (by less than two hours). The more substantial influence of the sea floor on nearshore plume evolution is through the bed stress. In the simulations, the bed stress decreases the cross-shore transport near the coast and causes water to be left behind when the plume separates from the coast. The idealized plume in the theory is unable to experience these dynamics and does not predict the jumps in plume properties at the time of separation from the coast.

An additional difficulty in comparing the Lentz theory with the simulations is the calculation of the bulk Richardson number. In principle, one could compute R_b from the model results. In practice, the computed values are very sensitive to the way that the plume base is defined. For the definitions used here, the case with no wave breaking had R_b between 2 and 3, although minor changes could give R_b less than 1. The simulations with

wave breaking had much larger values for R_b than the no-breaking simulations, which is consistent with the turbulence being generated by a mechanism other than shear instabilities.

Lentz's theory reproduces the numerical results of Fong and Geyer (2001) much better than it reproduces the results of this study, even in a no-breaking case when the Lentz theory is initialized using values after separation from the coast. This indicates differences between the Fong and Geyer simulations and the no-breaking simulation in this study. Reasons for these differences are not immediately obvious. Three possibilities are geometry, grid resolution, and turbulence closure. The Fong and Geyer simulations used a deeper coastal wall, so that the plume was not attached to the bottom and was less affected by bottom boundary layer turbulence. This surface-trapped geometry is much more similar to the Lentz geometry than is the bottom-attached geometry in our simulations. However, after the plume has detached from the coast and the water is sufficiently deep, one might expect these geometric differences to be less important. A second difference between Fong and Geyer (2001) and this study is grid resolution, both horizontal and vertical. This study uses a model with near-surface grid spacing of about 20 cm in 25 m of water. In the model of Fong and Geyer, the authors write that near the surface "resolution is better than 1 m" (Fong and Geyer 2001, p. 1070). Cross-shore grid spacing was also a factor of 2–3 larger in the simulations of Fong and Geyer than in these simulations. It is possible that reduced vertical resolution in their model led to smoothed velocity and density fields that increased gradient Richardson numbers and reduced mixing. Finally, Fong and Geyer used the Mellor–Yamada turbulence closure (Mellor and Yamada 1982), and this study used k – ϵ (Jones and Launder 1972). Warner et al. (2005) showed that in some test simulations (although not the deepening of a surface boundary layer) turbulent diffusivities computed using Mellor–Yamada were smaller than those computed using k – ϵ by a factor of about 2. Smaller turbulent diffusivities would lead to slower vertical mixing of the plume and slower thickening rate. This is consistent with the discrepancy between this study, in which the plume thickened faster than Lentz's prediction, and Fong and Geyer's study, in which the plume thickened slightly slower than Lentz's prediction.

b. Plume widening

Kinematically, the widening of the plume is caused by the cross-shore speed of the offshore edge of the plume being larger than the cross-shore speed of the onshore edge. Prior to detachment from the coast, the plume in

the wave-breaking cases is thicker because of the enhanced turbulence. This increased thickness causes the plume front to move offshore less quickly and the plume to widen less quickly prior to detachment than the plume in the simulation with no wave breaking. After detachment, the main cause of plume widening appears to be a divergence of mean offshore Ekman velocities caused by constant Ekman transport but different plume thicknesses at the offshore and onshore edges (Fig. 9). In all simulations in this study [as well as those in Fong and Geyer (2001)], the plume is thinner at the offshore edge than at the onshore edge. This is distinct from the flat-bottomed plume of Lentz (2004). The thinner part of the plume moves faster than the thicker part of the plume, which causes the plume to widen and thin while conserving volume. The widening due to divergent Ekman velocities is

$$\Delta u_{\text{Ek}} = U_E \left(\frac{1}{h_f} - \frac{1}{h_n} \right), \quad (15)$$

where h_f is the thickness of the plume at the offshore edge, and h_n is the thickness of the plume at the onshore edge. For this study, plume thicknesses were estimated as the mean thickness of the first two grid cells inside the plume at each edge. This corresponds to the mean thickness of roughly the outermost 1000 m at each edge of the plume. The cause of the sloped bottom is not known, but there is a feedback that would cause an asymmetric plume to form from an initially symmetric plume with a deep middle and thinner edges. Under upwelling-favorable winds, if the trailing edge is thinner than the center, the trailing edge will move faster than the center, catching up to it. The thin offshore edge, on the other hand, will continue to move offshore faster than the thicker center.

Figure 9 shows results for two representative cases, one with no wave breaking (case 1) and one with moderate wave breaking (case 4). Other wave-breaking cases are qualitatively similar to case 4. For the majority of the simulation periods, Ekman widening accounts for more than 75% of the simulated widening of the plume. Toward the ends of the simulations, the simulated widening rate grows away from the Ekman divergence rate; it is not immediately obvious whether this is related to the age of the plume or the approach of the outer edge of the model domain.

One possible cause of widening unrelated to Ekman divergence is ageostrophic gravitational slumping caused by the cross-shore density gradient. Analysis of the terms in the cross-shore momentum budget show that in the upper offshore quadrant of the plume, shear stress

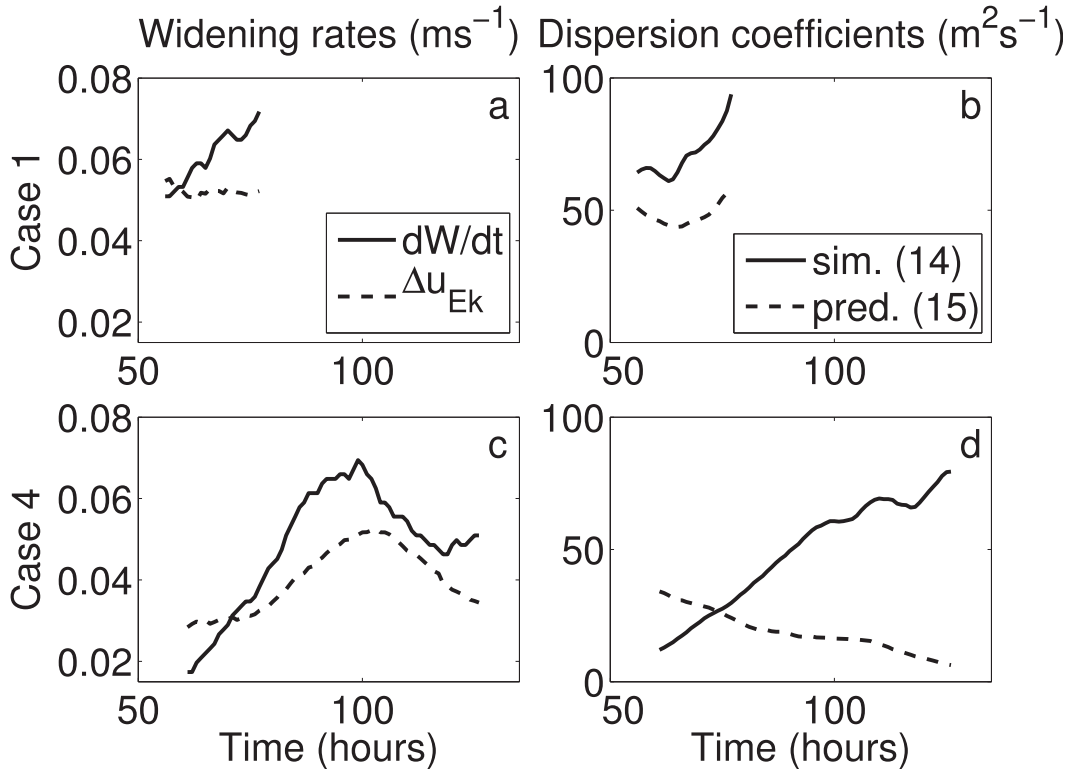


FIG. 9. (a),(c) Plume-widening rates for the simulation with no wave breaking (case 1) and moderate wave breaking (case 4). Case 4 is representative of the qualitative features in all of the wave-breaking simulations. Solid lines are the widening rate of the plume. Dashed lines are the widening rate expected from divergence of vertically averaged Ekman velocities in the plume (15). (b),(d) Horizontal dispersion coefficients for the simulation with no wave breaking (case 1) and with moderate wave breaking (case 4). The solid lines are K_x computed from the simulations using the second moment of the freshwater concentration and (16). The dashed lines are K_x predicted from vertical structures of K_z and u using (17). The data are filtered with a 24-h boxcar filter. The earliest time shown is the time of separation from the coast plus 24 h. The latest time shown is the time that the plume began to feel the effects of the offshore edge of the model domain.

is an important term balancing the pressure gradient (not shown). This is consistent with the notion of gravitational slumping. However, in all simulations, the other three quadrants show relationships more consistent with combinations of geostrophic and Ekman balances; the relationship between gravitational collapse and plume widening is unclear.

Another aspect of plume widening that has received attention in the past is shear dispersion. It is not a dynamical process in itself, but is the aggregate effect of multiple dynamical processes on a tracer patch. Shear dispersion plays a critical role in Lentz’s theory of plume widening. The results of this study suggest that it is much more important in simulations with no wave breaking than in simulations with wave breaking (Fig. 9). This is because shear dispersion is inversely related to the magnitude of the turbulent viscosity, which is much larger in the presence of wave breaking than in its absence.

Shear dispersion requires nonuniform vertical structure in the velocity and density fields and limited turbulent diffusivity (Bowden 1965). It will lead to increased volume of the plume and, unlike Ekman divergence, can widen the plume without thinning. To quantify the effects of shear dispersion, effective horizontal dispersion coefficients were computed from the simulations using two techniques: 1) the time rate of change of the second horizontal moment of the freshwater distribution (11), and 2) predicted from the vertical structures of velocity and turbulent viscosity in the plume (Bowden 1965). The horizontal dispersion coefficient is defined as (Fischer et al. 1979)

$$K_x = \frac{d}{dt} x_m^2. \tag{16}$$

Using the vertical structures of velocity and viscosity, Bowden (1965) predicts

$$K_x = \alpha \frac{u_s^2 h^2}{\max(K_z)}, \quad (17)$$

where u_s is the velocity at the surface,

$$\alpha = \frac{1}{h} \int_{-h}^0 dz' \left[f_1 \int_{-h}^{z'} dz'' \left(\frac{1}{g_1} \int_{-h}^{z''} dz''' f_1 \right) \right], \quad (18)$$

and f_1 and g_1 are vertical structure functions for velocity and viscosity, respectively. The function f_1 is the vertical structure of the horizontal velocity with its mean removed. For this analysis, the prediction of K_x was computed at all horizontal locations in the plume then averaged across the plume.

Comparison of K_x computed using (16) and (17) shows that shear dispersion is likely an important process in widening the plume with no breaking (Fig. 9). In the plume with wave breaking, however, shear dispersion may play a role early in the plume's development, but that role diminishes quickly as the plume moves offshore. Instead, the plume with breaking spreads in a more slab-like way than the plume with no breaking. This is caused by the large turbulent viscosity in the plume under breaking waves, which minimizes vertical gradients and causes shear dispersion to be weak as shown in (17).

c. Plume thickening

The rate of plume thickening is the result of competition between entrainment of ambient water and thinning caused by the widening processes discussed already. The thickening rate is the sum of two terms:

$$\frac{dh}{dt} = \overline{w_e} - \overline{w_t}, \quad (19)$$

where $\overline{w_e}$ is width-averaged entrainment, related to changes in cross-sectional area,

$$\overline{w_e} = \frac{1}{W} \frac{dA}{dt}, \quad (20)$$

and $\overline{w_t}$ is the thinning rate caused by plume widening with a constant cross-sectional area,

$$\overline{w_t} = \frac{h}{W} \frac{dW}{dt}. \quad (21)$$

Positive values of w_e correspond to plume thickening (increasing h) and positive values of w_t correspond to plume thinning (decreasing h).

Entrainment rates are of similar magnitude in all simulations and thinning rates are of similar magnitude

in all simulations. For the no-breaking case, the entrainment rates are on the high side of the distribution of entrainment rates and the thinning rates are on the low side of the distribution of thinning rates. Combined, these lead to faster plume thickening (by a factor of about 2) in the no-breaking case after the plume is detached from the coast (Fig. 10). However, because of differences prior to detachment, overall plume thickness is larger for the cases with wave breaking throughout the simulations.

A kinematic reason explains the fact that the thinning rate $\overline{w_t}$ is similar in all simulations, even though the plume with no breaking widens faster. The plume in the no-breaking case is wider and thinner than the plume in breaking cases. According to (21), this allows rapid widening without rapid thinning.

Given the substantially more energetic turbulence in the wave-breaking simulations, the similarity of entrainment rate $\overline{w_e}$ in the simulations with and without breaking is surprising at first. Indeed, prior to detachment the plume in wave-breaking simulations deepens more quickly than the plume in the simulation without wave breaking. When the plume is relatively thin, the enhanced TKE and turbulent diffusivity in simulations with wave breaking are able to entrain water more quickly. After separation, however, the wave-breaking simulations have a much thicker plume than the no-breaking simulation. In unstratified models, excess turbulent kinetic energy associated with wave breaking diminishes with depth and effectively vanishes by a depth of about ten times the significant wave height or about 15–20 times z_0 (Burchard 2001; Gerbi et al. 2009), and even at those depths the enhancement is small. In the simulations with wave breaking, the depth of the plume base is 10–20 times z_0 , and the results show that the enhancement of TKE and diffusivity due to wave breaking are much smaller near the plume base than they are near the surface (Fig. 6). If entrainment is occurring through the plume base rather than the plume front, this lack of extreme excess TKE is a possible explanation for the finding that the plume-average entrainment rates are similar in all simulations (Fig. 10). Although the wave breaking injects considerable energy into the plume, if the plume is thick enough, most of the additional energy is dissipated before it reaches the plume base and little energy is left for enhanced entrainment.

d. Effects of the coastal wall

The model domain used in this study was initially chosen for simplicity and numerical stability. An unanticipated result is that the offshore characteristics of the buoyant plume in upwelling-favorable winds are

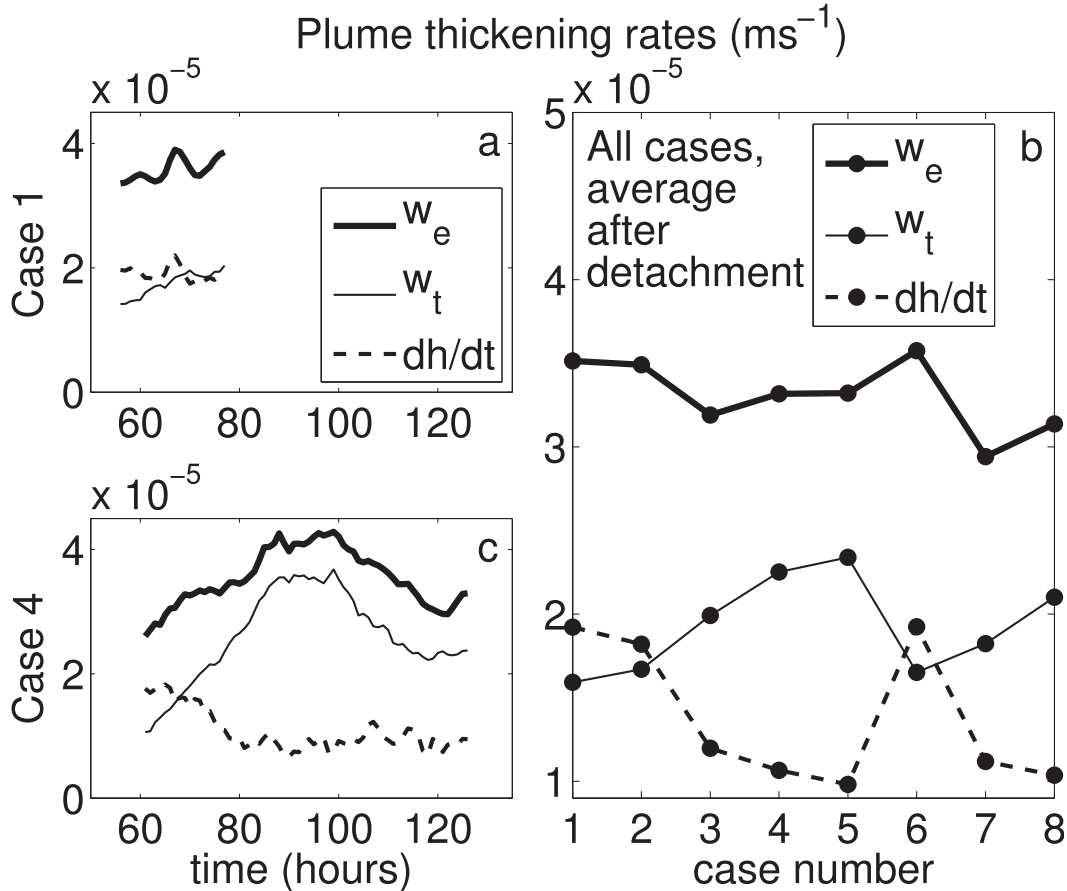


FIG. 10. Rates of plume thickening. (a),(c) Time series for cases with and without wave breaking are shown. (b) The average rates for each simulation between 12 h after the plume separated from the coast and the time that it began to be affected by the offshore boundary of the model. Case 1 has no wave breaking and in cases 2 and 6 wave breaking has been included in only one of the parameters (roughness length or energy input). Thick lines show \bar{w}_e . Thin lines show \bar{w}_t . Dashed lines show the thinning rate $dh/dt = w_e - w_t$. The data in the left column are filtered with a 24-h boxcar filter. The earliest time shown is the time of separation from the coast plus 24 h. The latest time shown is the time that the plume began to feel the effects of the offshore edge of the model domain.

affected substantially by the evolution of the plume while it is still attached to the coast. The presence of a coastal wall is likely to have some influence on the plume, particularly in the velocity structure near the wall, but it is possible that the wall does not alter the first-order dynamics of mixing, thickening, and widening. Prior to the onset of wind, the simulated plume base intersects the seafloor about 5-km offshore of the wall. This is of the same order as the deformation radius. According to the classification of Avicola and Huq (2002), the plume is initially bottom trapped, although the part of parameter space occupied by the plume was not explored by those authors. In simulations and laboratory experiments for which there is no appreciable coastal wall, both Garvine (2001) and Lentz and Helfrich (2002) suggest that most of the along-shelf

transport happens in the part of the plume offshore of where the sloping isopycnals first intersect the bottom. Garvine does point out some changes in salinities and transports in cases with a deeper coastal wall, but the overall structure of the simulations with a coastal wall is similar to that without a wall, but with the inner wedge of slow-flowing water removed.

In the study discussed here, the foot of the plume, where the plume base intersects the seafloor, is at a depth of about 15 m. Using the simulated downshelf plume transport and density, the scaling of Yankovsky and Chapman (1997) and Lentz and Helfrich (2002) predicts a depth of about 12 m, which is on the sloping part of the shelf in this domain. Augmenting the transport to allow for some downshelf flow in the wedge eliminated by the wall would increase this depth by up to

one meter. Thus, with the wall, the simulations have the foot of the plume about 2–3-km offshore and 2–3-m (20%) deeper than would be expected based on the scaling for a bottom that slopes steadily back to the shore. Importantly, the plume foot in both the scaling and simulations is offshore of the wall. In the simulations, freshwater is left behind on the shelf as the plume advects offshore. This limited cross-shelf transport suggests that the water depth in the simulation is smaller than likely depths of frictional influence (Ekman 1905; Madsen 1977). We interpret this to mean that with respect to cross-shelf transport caused by along-shelf winds, the model has an effective coastal wall at depths set by the Ekman layer thickness. This effective wall is in deeper water than the inshore edge of the model domain, and the coastal wall of the model may not play a major role in the response of the plume to along-shelf winds [see Fewings et al. (2008) for a discussion of effects of along-shelf winds on inner-shelf circulation]. The fact that the base of the plume at the time of detachment is at a depth similar to the wall depth does suggest that caution is necessary in this interpretation and that future simulations should examine this more closely.

5. Conclusions

This study examines both the dynamics of a buoyant plume during upwelling-favorable winds and the effects of turbulence related to wind-driven wave breaking on plume evolution. Inclusion of wave breaking in the turbulence parameterization has nonnegligible effects on plume evolution. Specifically, the plume with wave breaking is thicker and narrower than the plume without wave breaking. The different thicknesses lead to differences in the rate at which the plume is blown offshore. These differences are likely to have effects on real-world circulation and on numerical models with limited cross-shore domains.

In all simulations, after detachment from the coast, the plume widens dominantly through Ekman divergence. Even with this widening, the plume thickens throughout the simulations because entrainment rates are faster than thinning rates related to widening.

In simulations that include wave breaking, the plume is much more vertically homogeneous than the no-breaking plume. This increased vertical homogeneity suppresses the role of shear dispersion as the plume widens in simulations that include wave breaking.

In parameterizing the wave breaking, both the surface roughness and the TKE flux across the sea surface must increase from their no-breaking values. Within realistic parameter ranges, the above effects

are magnified as either roughness length or TKE flux is amplified.

The Richardson number-based theory of Lentz (2004) does a reasonable job of predicting rates of many aspects of plume evolution, but it does not capture the details of the detachment of the plume from the coast and it underpredicts the rate of plume thickening.

The wave-breaking parameterization used in this study is a simple one that can be easily incorporated into numerical models without simulating the full wave field. The fact that including this parameterization leads to changes in the circulation suggests that further study of this and other wave parameterizations is warranted in future work.

Acknowledgments. Funding for this work was provided by the Rutgers University Institute of Marine and Coastal Sciences Postdoctoral Fellowship and by U. S. National Science Foundation awards OCE-0238957 and OCE-0825833. Joe Jurisa graciously supplied the model grid and forcing. Eli Hunter and Weifang Zhang gave considerable technical help in the early stages of this work. John Warner aided in the understanding the numerical details of the turbulence parameterizations, and Hernan Arango gave much appreciated assistance and guidance. Conversations with Rocky Geyer and Steve Lentz and the comments of an anonymous reviewer strengthened this manuscript.

REFERENCES

- Agrawal, Y. C., E. A. Terray, M. A. Donelan, P. A. Hwang, A. J. Williams, III, W. M. Drennan, K. K. Kahma, and S. A. Kitaigorodskii, 1992: Enhanced dissipation of kinetic energy beneath surface waves. *Nature*, **359**, 219–220.
- Anis, A., and J. N. Moum, 1995: Surface wave-turbulence interactions: Scaling $\epsilon(z)$ near the sea surface. *J. Phys. Oceanogr.*, **25**, 2025–2044.
- Ardhuin, F., N. Raschle, and K. Belibassakis, 2008: Explicit wave-averaged primitive equations using a generalized Lagrangian mean. *Ocean Modell.*, **20**, 35–60.
- Avicola, G., and P. Huq, 2002: Scaling analysis for the interaction between a buoyant coastal current and the continental shelf: Experiments and observations. *J. Phys. Oceanogr.*, **32**, 3233–3248.
- Bowden, K. F., 1965: Horizontal mixing in the sea due to a shearing current. *J. Fluid Mech.*, **21**, 83–95.
- Burchard, H., 2001: Simulating the wave-enhanced layer under breaking surface waves with two-equation turbulence models. *J. Phys. Oceanogr.*, **31**, 3133–3145.
- , and K. Bolding, 2001: Comparative analysis of four second-moment turbulence closure models for the oceanic mixed layer. *J. Phys. Oceanogr.*, **31**, 1943–1968.
- Carniel, S., J. C. Warner, J. Chiggiato, and M. Sclavo, 2009: Investigating the impact of surface wave breaking on modeling the trajectories of drifters in the Northern Adriatic Sea during a wind-storm event. *Ocean Modell.*, **30**, 225–239.

- Chapman, D. C., 1985: Numerical treatment of cross-shelf open boundaries in a barotropic coastal ocean model. *J. Phys. Oceanogr.*, **15**, 1060–1075.
- Choi, B. J., and J. L. Wilkin, 2007: The effect of wind on the dispersal of the Hudson River plume. *J. Phys. Oceanogr.*, **37**, 1878–1897.
- Craig, P. D., 1996: Velocity profiles and surface roughness under breaking waves. *J. Geophys. Res.*, **101** (C1), 1265–1277.
- , and M. L. Banner, 1994: Modeling wave enhanced turbulence in the ocean surface layer. *J. Phys. Oceanogr.*, **24**, 2546–2559.
- Csanady, G. T., 1978: Wind effects on surface to bottom fronts. *J. Geophys. Res.*, **83**, 4633–4640.
- Drennan, W. M., M. A. Donelan, E. A. Terray, and K. B. Katsaros, 1996: Oceanic turbulence dissipation measurements in SWADE. *J. Phys. Oceanogr.*, **26**, 808–815.
- Ekman, V. W., 1905: On the influence of the earth's rotation on ocean currents. *Ark. Mat., Astron. Fys.*, **2**, 1–53.
- Feddersen, F., J. H. Trowbridge, and A. J. Williams III, 2007: Vertical structure of dissipation in the nearshore. *J. Phys. Oceanogr.*, **37**, 1764–1777.
- Fewings, M., S. J. Lentz, and J. Fredericks, 2008: Observations of cross-shelf flow driven by cross-shelf winds on the inner continental shelf. *J. Phys. Oceanogr.*, **38**, 2358–2378.
- Fischer, H. B., E. J. List, R. C. Y. Kho, J. Imberger, and N. H. Brooks, 1979: *Mixing in Inland and Coastal Waters*. Elsevier, 483 pp.
- Flather, R. A., 1976: A tidal model of the northwest European continental shelf. *Mem. Soc. Roy. Sci. Liege*, **6**, 141–164.
- Fong, D. A., and W. R. Geyer, 2001: Response of a river plume during an upwelling favorable wind event. *J. Geophys. Res.*, **106** (C1), 1067–1084.
- Garvine, R. W., 2001: The impact of model configuration in studies of buoyant coastal discharge. *J. Mar. Res.*, **59**, 193–225.
- Gemmrich, J. R., 2010: Strong turbulence in the wave crest region. *J. Phys. Oceanogr.*, **40**, 583–595.
- , T. D. Mudge, and V. D. Polonichko, 1994: On the energy input from wind to surface waves. *J. Phys. Oceanogr.*, **24**, 2413–2417.
- Gerbi, G. P., J. H. Trowbridge, J. B. Edson, A. J. Plueddemann, E. A. Terray, and J. J. Fredericks, 2008: Measurements of momentum and heat transfer across the air–sea interface. *J. Phys. Oceanogr.*, **38**, 1054–1072.
- , —, E. A. Terray, A. J. Plueddemann, and T. Kukulka, 2009: Observations of turbulence in the ocean surface boundary layer: energetics and transport. *J. Phys. Oceanogr.*, **39**, 1075–1096.
- Haidvogel, D. B., and Coauthors, 2008: Ocean forecasting in terrain-following coordinates: Formulation and skill assessment of the regional ocean modeling system. *J. Comput. Phys.*, **227**, 3595–3624.
- Hasselmann, K., 1970: Wave-driven inertial oscillations. *Geophys. Fluid Dyn.*, **1**, 463–502.
- Houghton, R. W., C. E. Tilburg, R. W. Garvine, and A. Fong, 2004: Delaware River plume response to a strong upwelling-favorable wind event. *Geophys. Res. Lett.*, **31**, L07302, doi:10.1029/2003GL018988.
- Jones, N. L., and S. G. Monismith, 2008: Modeling the influence of wave-enhanced turbulence in a shallow tide- and wind-driven water column. *J. Geophys. Res.*, **113**, C03009, doi:10.1029/2007/JC004246.
- Jones, W. P., and B. E. Launder, 1972: The prediction of laminarization with a two-equation model of turbulence. *Int. J. Heat Mass Transfer*, **15**, 301–314.
- Jurisa, J. T., and R. J. Chant, 2013: Impact of offshore winds on a buoyant river plume system. *J. Phys. Oceanogr.*, in press.
- Kantha, L. H., and C. A. Clayson, 1994: An improved mixed layer model for geophysical applications. *J. Geophys. Res.*, **99** (C12), 25 235–25 266.
- Kumar, N., G. Voulgaris, J. C. Warner, and M. Olabarrieta, 2012: Implementation of the vortex force formalism in the coupled ocean-atmosphere-wave-sediment transport (COAWST) modeling system for inner shelf and surf zone applications. *Ocean Modell.*, **47**, 65–95.
- Large, W. G., J. C. McWilliams, and S. C. Doney, 1994: Oceanic vertical mixing: A review and a model with a nonlocal boundary layer parameterization. *Rev. Geophys.*, **32**, 363–403.
- Lentz, S. J., 2004: The response of buoyant coastal plumes to upwelling-favorable winds. *J. Phys. Oceanogr.*, **34**, 2458–2469.
- , 2008: Observations and a model of the mean circulation over the Middle Atlantic Bight continental shelf. *J. Phys. Oceanogr.*, **38**, 1203–1221.
- , and K. R. Helfrich, 2002: Buoyant gravity currents along a sloping bottom in a rotating fluid. *J. Fluid Mech.*, **464**, 251–278.
- , M. Fewings, P. Howd, J. Fredericks, and K. Hathaway, 2008: Observations and a model of undertow over the inner continental shelf. *J. Phys. Oceanogr.*, **38**, 2341–2357.
- Madsen, O. S., 1977: A realistic model of the wind-induced Ekman boundary layer. *J. Phys. Oceanogr.*, **7**, 248–255.
- McWilliams, J. C., E. Huckle, J.-H. Liang, and P. P. Sullivan, 2012: The wavy Ekman layer: Langmuir circulations, breaking waves, and Reynolds stress. *J. Phys. Oceanogr.*, **42**, 1793–1816.
- Mellor, G. L., and T. Yamada, 1982: Development of a turbulence closure model for geophysical fluid problems. *Rev. Geophys.*, **20**, 851–875.
- Noh, Y., H. S. Min, and S. Raasch, 2004: Large eddy simulation of the ocean mixed layer: the effects of wave breaking and Langmuir circulation. *J. Phys. Oceanogr.*, **34**, 720–735.
- Polton, J., D. Lewis, and S. Belcher, 2005: The role of wave-induced Coriolis–Stokes forcing on the wind-driven mixed layer. *J. Phys. Oceanogr.*, **35**, 444–457.
- Rodi, W., 1980: *Turbulence Models and Their Application in Hydraulics*. International Association for Hydraulic Research, 115 pp.
- Shchepetkin, A. F., and J. C. McWilliams, 2005: The regional oceanic modeling system (ROMS): A split-explicit, free-surface, topography-following-coordinate oceanic model. *Ocean Modell.*, **9**, 347–404.
- , and —, 2008: Computational kernel algorithms for fine-scale, multi-process, long-term oceanic simulations. *Handbook of Numerical Analysis, Vol. XIV: Computational Methods for the Ocean and the Atmosphere*, P. G. Ciarlet, R. Temam, and J. Tribbia, Eds., Elsevier Science, 121–183.
- , and —, 2009: Correction and commentary for “Ocean forecasting in terrain-following coordinates: Formulation and skill assessment of the regional ocean modeling system” by Haidvogel et al., *J. Comp. Phys.* **227**, pp. 3595–3624. *J. Comput. Phys.*, **228**, 8985–9000.
- Soloviev, A., and R. Lukas, 2003: Observation of wave-enhanced turbulence in the near-surface layer of the ocean during TOGA COARE. *Deep-Sea Res. I*, **50**, 371–395.
- Stips, A., H. Burchard, K. Bolding, H. Prandke, A. Simon, and A. Wüest, 2005: Measurement and simulation of viscous dissipation in the wave affected surface layer. *Deep-Sea Res. II*, **52**, 1133–1155.

- Sullivan, P. P., J. C. McWilliams, and W. K. Melville, 2007: Surface gravity wave effects in the oceanic boundary layer: Large-eddy simulation with vortex force and stochastic breakers. *J. Fluid Mech.*, **593**, 405–452.
- Teixeira, M. A. C., 2012: The influence of Langmuir turbulence on the scaling for the dissipation rate in the oceanic boundary layer. *J. Geophys. Res.*, **117**, C05015, doi:10.1029/2011JC007235.
- Terray, E. A., M. A. Donelan, Y. C. Agrawal, W. M. Drennan, K. K. Kahma, A. J. Williams III, P. A. Hwang, and S. A. Kitaigorodskii, 1996: Estimates of kinetic energy dissipation under breaking waves. *J. Phys. Oceanogr.*, **26**, 792–807.
- , W. M. Drennan, and M. A. Donelan, 1999: The vertical structure of shear and dissipation in the ocean surface layer. *Proc. Symp. on the Wind-driven Air-Sea Interface—Electromagnetic and Acoustic Sensing, Wave Dynamics, and Turbulent Fluxes.*, Sydney, Australia, University of New South Wales, 239–245.
- Uchiyama, Y., J. C. McWilliams, and A. F. Shchepetkin, 2010: Explicit wave-averaged primitive equations using a generalized Lagrangian mean. *Ocean Modell.*, **34**, 16–35.
- Umlauf, L., and H. Burchard, 2003: A generic length-scale equation for geophysical turbulence models. *J. Mar. Res.*, **61**, 235–265.
- , and —, 2005: Second-order turbulence closure models for geophysical boundary layers. A review of recent work. *Cont. Shelf Res.*, **24**, 795–827.
- Warner, J. C., C. R. Sherwood, H. G. Arango, and R. P. Signell, 2005: Performance of four turbulence closure models implemented using a generic length scale method. *Ocean Modell.*, **8**, 81–113.
- , —, R. P. Signell, C. K. Harris, and H. G. Arango, 2008: Development of a three-dimensional, regional, coupled wave, current, and sediment transport model. *Comput. Geosci.*, **34**, 1284–1306.
- Xing, J., and A. M. Davies, 1999: The effect of wind direction and mixing upon the spreading of a buoyant plume in a non-tidal regime. *Cont. Shelf Res.*, **19**, 1437–1483.
- Yankovsky, A. E., and D. C. Chapman, 1997: A simple theory for the fate of buoyant coastal discharges. *J. Phys. Oceanogr.*, **27**, 1386–1401.
- Zhang, W. G., J. L. Wilkin, and R. J. Chant, 2009: Modeling the pathways and mean dynamics of river plume dispersal in the New York Bight. *J. Phys. Oceanogr.*, **39**, 1167–1183.
- Zhang, X., G. Han, D. Wang, W. Li, and Z. He, 2011: Effect of surface wave breaking on the surface boundary layer of temperature in the yellow sea in summer. *Ocean Modell.*, **38**, 267–279.